Dislocation Structures, Interfacing, and Magnetism in the $L1_0$-MnGa on $\eta_\perp$-Mn_3N_2 Bilayer

J. P. Corbett, J. Guerrero-Sánchez, A.L. Richard, A.-O. Mandru, J. C. Gallagher, F. Yang, D. C. Ingram, N. Takeuchi, and A. R. Smith

Nanoscale and Quantum Phenomena Institute, Department of Physics and Astronomy, Ohio University, Athens, OH 45701, USA

,

Centro de Nanociencias y Nanotecnologia, Universidad Nacional Autónoma de México, Apartado Postal 14, Ensenada Baja California, Código Postal 22800, México.

,

Department of Physics, The Ohio State University, 191 Woodruff Avenue, Columbus, OH 43210, USA

Abstract

Ferromagnetic $L1_0$-MnGa was grown by molecular beam epitaxy under ultra-high vacuum conditions to a 73 ± 5 nm thickness atop of 50 ± 5 nm thick molecular beam epitaxy grown antiferromagnetic $\eta_\perp$-Mn_3N_2 on a MgO(001) substrate. The MnGa grew along the c-axis with an *out-of-plane* spacing of c = 3.71 ± 0.01 Å and a relaxed *in-plane* spacing of a = 4.00 ± 0.05 Å measured with X-ray diffraction and reflection high-energy electron diffraction respectively. Williamson-Hall analysis revealed 67 ± 17 nm tall columnar grains with a residual stress of 2.40 ± 0.26 ($\times 10^{-3}$). A radial distribution plot of screw dislocations observed in scanning tunneling microscopy images found an *in-plane* coherence length of 15 ± 5 nm. Reflection high-energy electron diffraction analysis of the *in-plane* lattice spacing during growth reveals a critical thickness of 1.05 ± 0.65 nm for the MnGa, by which the MnGa film relaxes by incorporating dislocations of both edge and screw type. Vibrating sample magnetometry was employed to obtain the magnetic properties of the bilayer system. It is found that the dislocation density plays a significant role in understanding the

measured moment per unit cell, where a large dislocation density lowers the moment per unit cell significantly due to chemical layering disorder. This finding is important for materials development of large saturation magnetization.

Keywords: MnGa, Mn_3N_3, interfaces, STM, edge dislocation, screw dislocation, density functional theory

2010 MSC: 00-01, 99-00

1. INTRODUCTION

The Mn-Ga system offers a variety of magnetic phases depending on the composition and structure. A variety of polymorphs of Mn-Ga exist, as a few examples, the ferrimagnetic tetragonal $D0_{22}$-Mn_3Ga, an antiferromagnetic hexagonal $D0_{19}$-Mn_3Ga, and the phase of interest to this work the ferromagnetic $L1_0$-MnGa[1, 2]. Recently, a strong interest in developing permanent magnets without the use of rare-earth elements has developed due to clean energy and national security demands[3]. Mn-based alloys offer an exciting and diverse possibility to fulfill these demands through the variety of magnetic phases and high tunability of magnetic properties[1, 4]. MnGa alloys have attractive attention as a candidate to fulfill this role as a rare-earth-free permanent magnet[5].

Additionally, MnGa alloys attracted significant attention for use in nanoscale spintronic devices due to their perpendicular magnetic anisotropy (PMA) with a uniaxial anisotropy constant (K_u) as high as 20 Merg/cm^3 and high Curie point of 350 °C[4, 5, 6, 7]. A tailorable saturation magnetization (M_s) is important for creating non-interacting, but high signial-to-noise storage bits[4]. Understanding what growth conditions and crystal quality impact the magnetic properties is integral to bringing these materials to maturity as devices.

For our investigations we focus on the ferromagnetic $L1_0$-MnGa, a tetragonal system consisting of equal parts Mn and Ga. When a high quality crystal is prepared, a layered structure of alternating sheets of Mn and Ga form along (001)[4].

The growth and magnetism of $L1_0$-MnGa on semiconductors like GaN, and

GaAs are well documented with a good lattice matching for growth along the [111] direction[4, 8, 9]. By altering the concentration of Ga in these systems, multiphase Mn-Ga crystals can develop with strong consequences on the magnetic properties of the film[10]. Growth on insulators like MgO(001) and sapphire(111) have been studied previously with growth orientations of [100] or [110][9, 11, 12]. A review detailing the growth and magnetism of $L1_0$-MnGa and related $D0_{22}$ on various substrates is given by Li-Jun *et al.*[4]. Despite the well-documented growth and magnetism of Mn-Ga phases in thin films, the dislocation structures of these compounds remain unexplored with only a few studies reporting observations of dislocations as part of larger studies.

Zheng *et al.* investigated the impact of molecular beam epitaxy (MBE) growth parameters on the full-width at half-maximum (FWHM) of X-ray diffraction (XRD) patterns which are related to the dislocation density of the material; although the researchers did not address this relationship directly a build-up of edge dislocations was observed in atomic force microscopy (AFM)[11]. Other studies uncovered grain structures in high-resolution transmission electron microscopy images of the $D0_{22}$ structure[6]. However, overall the literature remains lacking in studies involving atomic observations of dislocations in MnGa compounds.

Magnetic bilayers utilizing exchange bias (EB) are of great technological interest[13]. However, the EB phenomenon has yet to be fully understood[14, 15, 16]. A bilayer of ferromagnetic $L1_0$-MnGa and antiferromagnetic (aFM) $\eta_{\perp}$-Mn_3N_2 offers the possibility to explore unconventional EB ($T_N \leq T_C$) effects above room temperature. The exploration of unconventional EB systems with the traditional paradigm of $T_N \leq T_C$ being reversed looks at interesting temperature effects, and even the persistence of EB into the paramagnetic state[15, 17]. Experimentally, EB is highly dependent on the experimental growth conditions, the materials of choice, and physical conditions of the sample. Preparing novel systems for possible EB measurements first requires an understanding of the interfacial structure, and the magnetism of the bilayer in question.

Mn_3N_2 is an interesting compound for potential spin device applications

and has been explored in detail chemically, crystallographically, and magnetically, even down to the atomic spin structure of the terminating surfaces via spin-polarized STM making it a good candidate for possible EB explorations[18]. Zilske *et al.* and Meinert *et al.* demonstrated giant EB in MnN heterostructures, motivating further investigations of the Mn_xN_y system for EB experiments prepared under MBE conditions[19, 20].

In this report, scanning tunneling microscopy (STM), and diffraction experiments are combined with density functional theory (DFT) calculations to investigate the interplay between the interface and disorder on the magnetic properties of MBE grown bilayer of $L1_0$-MnGa on aFM $\eta_\perp$-Mn_3N_2. We determine a significant impact of the dislocation density on the magnetic ordering of the solid. Where a high dislocation density nearly halves the measured moment per unit cell (i.e.M_s). The interfacing between $L1_0$-MnGa and $\eta_\perp$-Mn_3N_2 is explored computationally leading to the understanding of the underlying mechanism between crystallographic disorder of the $L1_0$ layers and the magnetic ordering of the MnGa film. We also observe edge and screw type dislocations terminating on the surface via atomically resolved STM imaging and related these to the interfacing. These findings are important for the tailoring of magnetic properties for spintronic devices with a low M_s, or strong rare-earth-free magnets by uncovering some of the interplay between disorder and magnetism.

2. EXPERIMENTAL

The samples are grown by MBE in a ultra-high vacuum (UHV) system with a base pressure of 1.0×10^{-10} Torr. Epitaxial development during crystal formation is monitor in real-time with a 20 keV electron beam from a reflection high-energy electron diffraction system provided by Staib instruments. A custom-built room temperature scanning tunneling microscope (STM) and 5 keV Auger electron Spectrometer (AES) from Staib Instruments are operated in a separate UHV chamber that is coupled to the MBE growth chamber, allowing for *in-situ* growth and analyses under UHV conditions. The STM uses

electrochemically etch W tips for scanning[21]. Conductance mapping is performed using a lock-in amplifier to measure the first harmonic with a modulation bias ∼20 mV, and frequency of ∼1500 Hz. The MgO(001) substrate is annealed at 1100 ± 30 °C in a 2.0 × 10^{-5} Torr N plasma until the RHEED pattern is streaky indicating a smooth surface, see Fig.1(a). Deposition of $\eta_{\perp}$-Mn_3N_2 follows the work of Yang *et al.* with a substrate temperature of 400 ± 30 °C, a 2.0 × 10^{-5} Torr N plasma, and a Mn:N flux ratio of 0.40 ± 0.04[22]. The $\eta_{\perp}$-Mn_3N_2 deposition conditions are maintained until a 50 ± 5 nm film grows. Then the N plasma and Mn flux are terminated simultaneously, and the substrate cools to 325 ± 30 °C for MnGa deposition.

Fig. 1(b) shows the streaky RHEED pattern of the 50 ± 5 nm $\eta_{\perp}$-Mn_3N_2 indicating the prepared film is atomically smooth. The substrate temperate is maintained at 325 ± 30 °C for MnGa deposition with a flux ratio of Mn:Ga = 1.0 ± 0.1 until 73 ± 5 nm thick film forms. The Mn and Ga fluxes are then terminated and the sample cools to room temperature prior to transfer in UHV to the STM or AES for analysis.

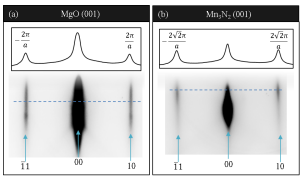

Figure 1: *In-situ* RHEED images of MgO(001) and epitaxially grown $\eta_{\perp}$-Mn_3N_2. (a) Streaky RHEED pattern of annealed MgO(001) along the <100> direction. (b) image of 50 nm thick $\eta_{\perp}$-Mn_3N_2 RHEED along the <100> substrate direction showing an atomically smooth Mn_3N_2(001) film. Line profiles of the RHEED patterns are shown as insets.

Ex-situ analyses are carried out with a Bragg-Brentano θ–2θ XRD system from Rigaku with a Cu Kα x-ray source. Bulk compositional measurements are taken with a Rutherford backscattering spectrometer (RBS) system using a 4.5-MV tandem accelerator with measurements made using 2.2 MeV and 3.035 MeV alpha beams. Vibrating sample magnetometry (VSM) measurements are carried out at room temperature with a max field of ±16 KOe. The specimens

are cut such that the center ($\sim$0.5 $\times$ $\sim$0.5 cm^2) of the as-grown film are used in VSM measurements.

The error in the sample temperature during MBE growth is determined from calibration curves of a thermocouple mounted behind the substrate and a pyrometer focused on the front of the sample. The fluxes are determined using a quartz balance thickness monitor with errors in the fluxes determined from the standard deviation of several flux measurements for a particular temperature. The N flux is estimated using the crossover point between Ga and N rich growth conditions for a GaN film[23].

The DFT calculations are preformed using spin-polarized first principles and are carried out with the PWscf code of the Quantum ESPRESSO package[24]. The electronic states are expanded in delocalized plane waves with a kinetic energy cutoff of 30 Ry. The charge density expansion is truncated at 240 Ry. The non-classical electronic interactions are treated with the generalized gradient approximation, as implemented in the Perdew-Burke-Ernzerhof parametrization[25]. Core electrons are treated using ultra-soft pseudopotentials[26]. To evaluate the Brillouin zone integrations, we use a k-points mesh of 6 $\times$6 $\times$ 1[27]. Every interface model is fully relaxed until the force and energy criteria of 0.001 Ry/a.u. and 0.0001 Ry are accomplished, respectively. Such criteria are sufficient to account for different magnetic alignments at the interface.

3. DISCUSSION

3.1. Growth and Interface

In Fig. 2(a) a plot of the *in-plane* lattice spacing versus thickness for the MnGa film is shown. The bulk *in-plane* lattice of $L1_0$-MnGa is 3.88 Å, while MnGa initially nucleates with a larger than bulk *in-plane* lattice to be commensurate to the $\eta_{\perp}$-Mn_3N_2 until a critical thickness of 1.05 $\pm$ 0.65 nm is reached, as seen by the step in Fig. 2(a). The width of the transition region in the step is used as the error in the critical thickness. After the critical thickness,

the MnGa relaxes to a slightly larger than bulk *in-plane* spacing by dislocation incorporation into the film[28].

The evolution of the [100] RHEED direction from commensurate layers to the Stranski-Krastanov (layer-plus-island growth) and finally to layer-by-layer growth is presented as a series of [100] patterns shown in Fig. 2(b), as taken along the data in part (a)[29]. This qualitative evolution of the RHEED pattern indicates that the $L1_0$-MnGa growth undergoes a transition from layer-plus-island growth to a strictly layer growth after a thickness of 55.0 ± 5.0 nm. Figure 2(c,d) shows the RHEED patterns of the 73.0 ± 5.0 nm MnGa film along the [100] and [110] MgO directions at the growth temperature. From the primary RHEED streaks along the [100] and [110] directions, the ratio of the streak spacing of [100] to [110] directions results in a $\sqrt{2}$ indicating that the MnGa grows without rotation with respect to the Mn_3N_2 substrate resulting in the epitaxial relation [100] MnGa ∥ [100] Mn_3N_2.

The $\eta_\perp$-Mn_3N_2 surface is morphologically made up of nano-pyramid shapes with three unique chemical terraces[10, 18, 30]. For growth along the [001] direction, MnGa has two possible chemical layers, either a Mn or a Ga layer. In order to understand the interfacing between MnGa and Mn_3N_2 theory is needed to untangle how the MnGa is stable atop of the $\eta_\perp$-Mn_3N_2. The three possible different $\eta_\perp$-Mn_3N_2 terminations are: a Mn-MnN-Mn-MnN terminated surface (model A1), a Mn-MnN-MnN terminated surface (model B), and a Mn-MnN terminated structure (model C)[30]. The models A1, B, and C are composed of 9, 8, and 7 monolayers, respectively. The MnGa films which are deposited on top of each substrate (A1, B, and C) are (x-MnGa-y, in which, x = interface layer, and y = surface layer): Mn-MnGa-Mn is labeled model 1, Ga-MnGa-Ga which is model 2, Ga-MnGa-Mn is model 3, and Mn-MnGa-Ga which is model 4. Therefore, the interfaces are combinations of A1, B, and C with x-MnGa-y (e.g. A1-1 is a bilayer between Mn-MnN-Mn-MnN and Mn-MnGa-Mn). Also, we are taking advantage of the inversion symmetry, so then, two equivalent surface terminations and two interfaces are present [31]. Shown in Fig. 3(d) the MnGa preferentially begins growth with Mn-layers atop of the nano-pyramids

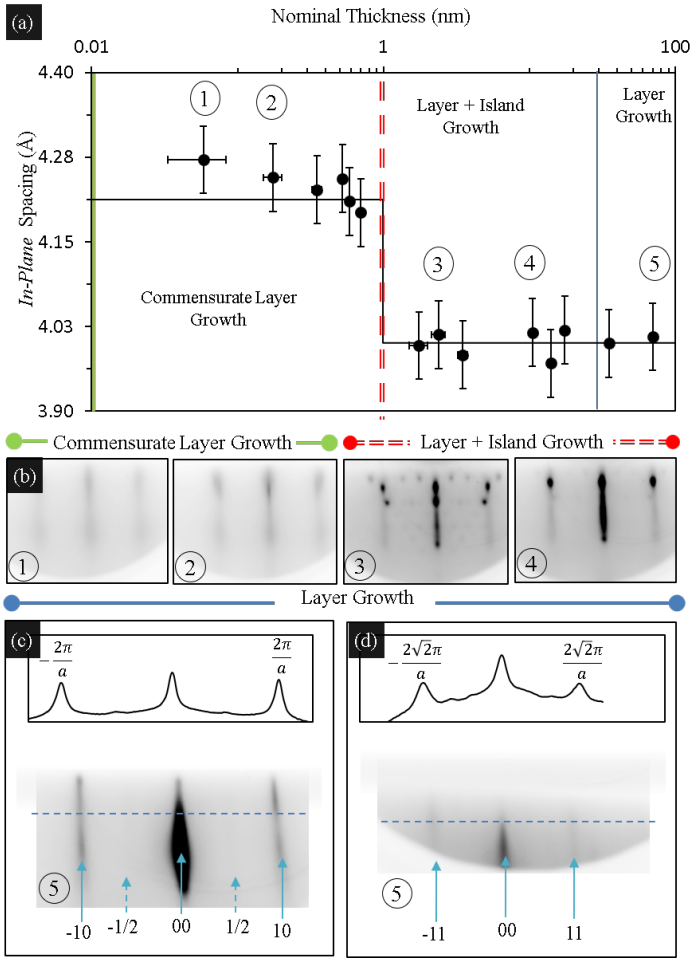

Figure 2: (a) *In-plane* lattice measurements from RHEED of the <100> direction versus thickness show a distinct critical thickness at 1.05 nm. Prior to relaxation, the MnGa is commensurate to the Mn_3N_2 *in-plane* lattice. After the critical thickness, the MnGa film relaxes to a*in-plane* spacing closer to the bulk spacing. (b) A series of [100] RHEED images of MnGa showing the growth evolution along the data in (a) marked numerically. The film has a three stage transition from commensurate layer growth, to layer-plus-island growth, and finally to layer-by-layer growth. (c) Streaky RHEED image along the [100] direction at the end of growth. (d) Corresponding streaky RHEED of <110> direction of the MnGa at the end of growth.

and then begins to order in alternating Ga and Mn layers.

In order to describe the thermodynamic stability of the interfaces we use

the interface formation energy formalism [31, 32]. Such formalism has been developed in detail for magnetic interfaces in the work by J. Guerrero-Sanchez et. al [31]. The interface energy ($\Lambda^{f}_{\frac{MnGa}{Mn_3N_2}}$ as a function of $\Delta\mu(1) = 3\mu_{Mn} - 2\mu_N$ and $\Delta\mu(2) = \mu_{Mn} - \mu_{Ga}$ can be written as:

$$\Lambda^{f}_{\frac{MnGa}{Mn_3N_2}} = \frac{\Delta E_{Int}}{2A} + \frac{1}{2A}\{E^{Slab}_{Mn_3N_2} - \frac{1}{2}(\frac{n_{Mn}}{3} + \frac{n_N}{2})\mu^{bulk}_{Mn_3N_2} - \frac{1}{2}(\frac{n_{Mn}}{3} - \frac{n_N}{2})\Delta\mu(1)\}$$
$$+\frac{1}{2A}\{E^{Slab}_{MnGa} - \frac{1}{2}(n_{Mn} + n_{Ga})\mu^{bulk}_{MnGa} - \frac{1}{2}(n_{Mn} - n_{Ga})\Delta\mu(2)\} \quad (1)$$

where ΔE_{Int} is the total energy of the interface, $E^{Slab}_{Mn_3N_2}$ and E^{Slab}_{MnGa} are the total energies of the Mn_3N_2 and MnGa surfaces respectively, A is the surface area in each case, $\mu^{bulk}_{Mn_3N_2} = 3\mu^{bulk}_{Mn} + 2\mu^{bulk}_{N}$ and $\mu^{bulk}_{MnGa} = \mu^{bulk}_{Mn} + \mu^{bulk}_{Ga}$ are the chemical potentials of the bulk Mn_3N_2 and MnGa respectively, and finally n_i is the number of atoms of the i^{th} species (Mn, N, and Ga). The $\Lambda^{\frac{MnGa}{Mn_3N_2}}$ can be plotted only in the following limits: $-\Delta H^{Mn_3N_2}_f \leq \Delta\mu(1) \leq \Delta H^{Mn_3N_2}_f$ and $-\Delta H^{MnGa}_f \leq \Delta\mu(2) \leq \Delta H^{MnGa}_f$ where ΔH^{xy}_f is the formation enthalpy of each compound (x and y). The upper and lower limits correspond to Mn-rich and N-rich or Ga-rich conditions, respectively.

As mentioned before, the interface models are constructed by combining the substrates (A1, B, and C) with all the possible films (x-MnGa-y). For example, A1-1 is an interface formed by an A1 substrate and the Mn-MnGa-Mn film; the film is Mn initiated, has alternating Mn and Ga layers and then is Mn terminated. After fully relaxing all the possible combinations between substrate-film models, we have found only three stable interfaces labeled A1-4, B-4, and C-4, as shown in Fig. 3(c). They are the combinations of A1, B, and C substrates with film 4 (the Mn-MnGa-Ga film). The A1-4 interface is stable for very Mn-rich conditions of $\Delta\mu(1)$, while the C-4 and B-4 interfaces are stable for progressively lower Mn chemical potential as seen in Fig. 3(b). It is important to mention that all stable models are favorable for all ranges of $\Delta\mu(2)$ if we only consider 1×1 surface structures, see Fig. 3(b).

As previously established in detail, $L1_0$-MnGa (001) has two possible ter-

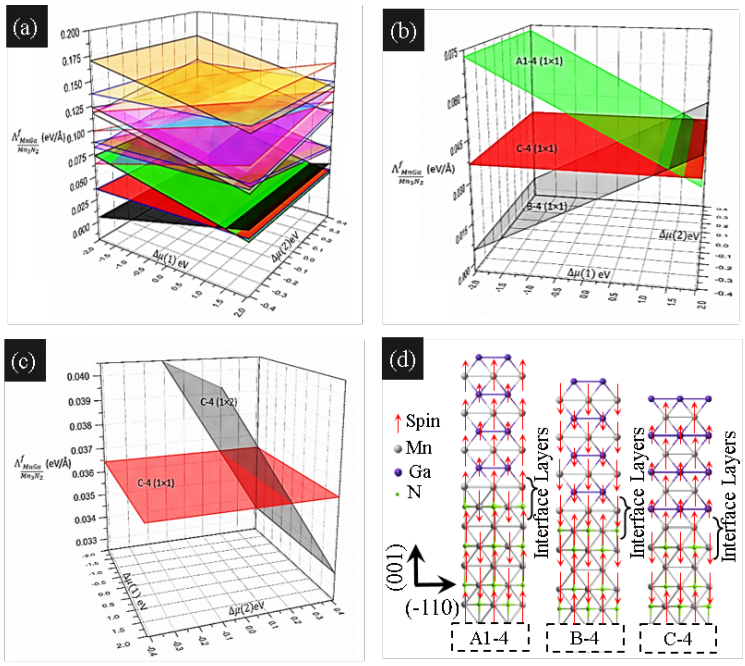

Figure 3: 2D formation energy plots and equilibrated interfaces for the different combinations x-MnGa-y on A1, B, and C Mn_3N_2 terminations. (a) All considered x-MnGa-y models with a 1×1 surface termination. (b) 2D formation energy plots of the most energetically stable 1×1 Ga-MnGa-Mn interfaces on each of the three Mn_3N_2 terminations. (c) 2D formation energy plot comparison of the 1×1 Ga termination versus the 1×2 Mn/Ga substituted Ga terminaton grown atop of the C Mn_3N_2 termination. (d) Epitaxial models of the most stable energy configurations for all three Mn_3N_2 (001) terminations.

minations, a Ga-terminated 1×1 and a 1×2 with Mn substituting Ga at 1/4 of the surface Ga sites.[31, 33]. To verify that the 1×2 Mn/Ga substituted 1×1 Ga surface is stable, we compare the energy of the C-4 interface having a terminating 1×2 surface structure to that of a simple 1×1 Ga termination. After full relaxation of the two surfaces, we see that the C-4 1×2 model is more stable than the C-4 1×1 model for Mn rich conditions of $\Delta\mu(2)$, as seen in Fig. 3(c).

These results demonstrate that MnGa can directly grow on Mn_3N_2, where the interfaces are formed by a MnN layer of the substrate and a Mn layer of the film. Thus, solidifying the multifaceted epitaxial relationship and formation of

this bilayer system.

3.2. Dislocation Structures

Figure4(a) x-ray spectrum shows the 001 peak at $2\theta = 23.98 \pm 0.01$ degrees, the 002 peak at 49.01 ± 0.01 degrees, and the 004 peak at 112.29 ± 0.05 degrees, corresponding to the 001 direction with an *out-of-plane* lattice constant (c) equal to 3.71 ± 0.01 Å. The error in c is determined from the peak positions in 2θ of the 001 family of peaks using Braggs law. Rutherford backscattering confirms a stoichiometric phase with a compositional ratio Mn:Ga = 1.01 ± 0.15, with the error in the composition determined from the goodness of the fit to the RBS intensity-energy profile. We rule out $D0_{22}$-Mn_3Ga since the composition of this phase (Mn:Ga of 3:1) deviates too much from our measured value.

The observation of 002 and 004 higher order reflections is indicative of the layering superstructure of alternating Mn and Ga layers in a pure phase growth of $L1_0$-MnGa[5]. However, it should be noted that growth of a stoichiometric MnGa film is possible with a so-called disordered phase lacking the alternating Mn and Ga planes of atoms while retaining the overall tetragonal structure[5, 28, 34, 35]. In our XRD spectrum we lack the observation of the 003 peak which suggests that we do not have a highly ordered layered structure, but instead a mixture between well-ordered layers and some disordered layering[5].

Our calculations of the interface formation guide our understanding of the layer disordering. The $\eta_\perp$-Mn_3N_2 forms a nano-pyramidal morphology with a terrace width of approximately 10–20 nm and a nominal step height of 2.0 Å[36]. In Fig. 5(a) the three possible Mn_3N_2 terraces are shown along the [110] with alternating Mn and Ga layers atop of it in accordance with our theory calculations. Going across a step edge of A1 to B, B to C, and C to A1 it is clear that the second layer (Ga) from the A1 surface is leveled with the third (Mn) layer from the B surface and with the fourth (Ga) layer from C and so on..

In the $L1_0$-MnGa structure, the Ga layer is geometrically the same as the Mn layer but with an apparent lateral shift of $[\frac{1}{2}\frac{1}{2}0]$ relative to the Mn layer. When

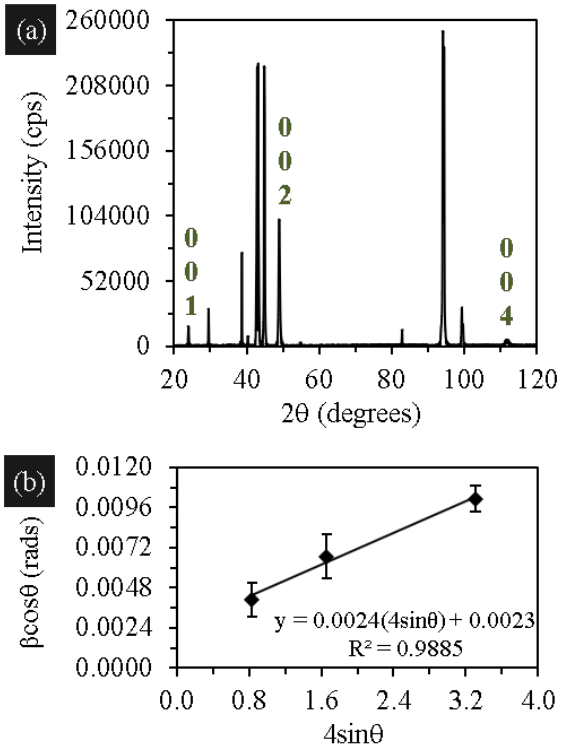

Figure 4: (a) XRD pattern revealing a single-oriented MnGa(001) film. Additional peaks are from the MgO substrate and the Mn_3N_2(001) film. (b) Williamson-Hall plot of the 001, 002 and 004 peaks of MnGa.

stepping from one Mn_3N_2 terrace down (or up) to the next, the relative positions of the N atoms in the MnN terminating layer can be viewed as changing from corner atoms to edge-centered atoms, as shown in Fig. 5(b). This change in the relative positions of N atoms going across a Mn_3N_2 step is crucial, as this causes an effective $[\frac{1}{2}\frac{1}{2}0]$ shift relative to the adjacent terraces. The relative $[\frac{1}{2}\frac{1}{2}0]$ shift in N positions allows for a Mn layer to geometrically match with a Ga layer across a Mn_3N_2 step edge as shown in Fig. 5(c) causing only a chemical disordering.

A Williamson-Hall analysis of the 001, 002, and 004 peaks, consisting of plotting a factor $\beta\cos(\theta)$ versus $4\times\sin(\theta)$, is presented in Fig. 4(b), where β is the

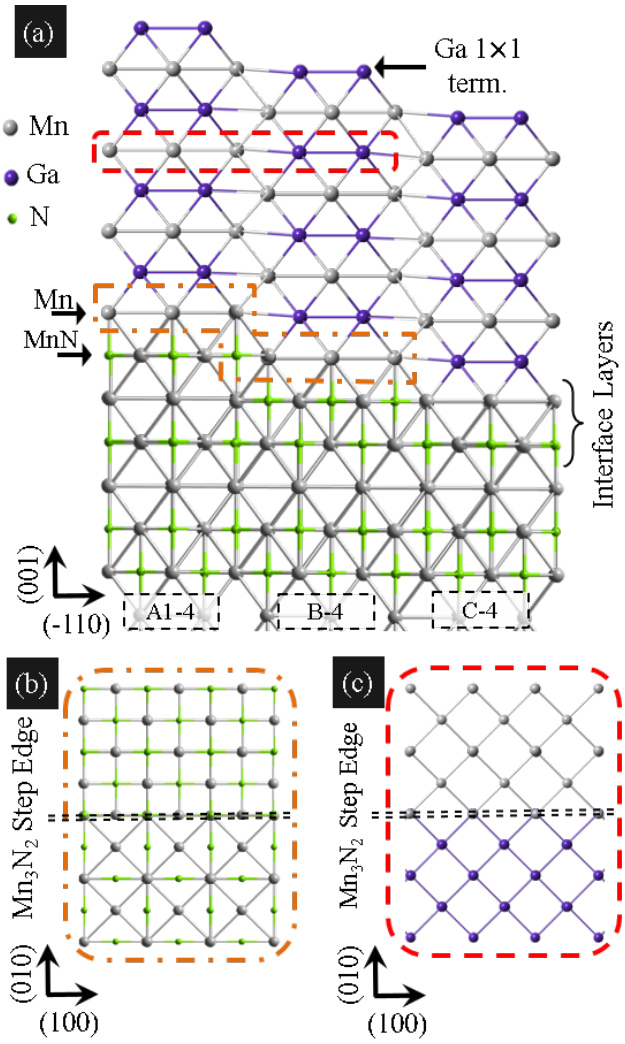

Figure 5: (a) Interfacing models across the adjacent steps in $Mn_3N_2(001)$ shown at <110>. Layering disorder in MnGa is shown here as a consequence of the Mn_3N_2 step heights from A1 to B, and B to C. The step from C to A1 is not shown, but would follow similarly to the other steps. The dashed lines indicate side-view features that are displayed as a top view in (b) and (c). (b) A top view of the Mn_3N_2 surface traversing from A1 to B showing the change in relative atomic positions of Mn and N after moving down one atomic step, and thereby altering the first layer Mn binding sites of MnGa. (c) A top-down view of a layer of MnGa which extends over a step edge of Mn_3N_2 to demonstrate the chemical layer mismatching.

integral broadening of the diffraction peak and θ is Bragg angle[37]. By plotting $\beta\cos(\theta)$ versus $4\times\sin(\theta)$ the slope is proportional to the *out-of-plane* coherence length $d_\perp$ and the intercept is the residual strain[38]. The Williamson-Hall analysis reveals tall columnar grains with an *out-of-plane* coherence length of $d_\perp = 67 \pm 17$ nm and a residual strain $\epsilon_\perp = 2.38 \pm 0.26(\times 10^{-3})$[37, 39]. Errors in the $d_\perp$ and strain are determined from the errors of linear regression. It is interesting the $d_\perp$ is in good agreement with the thickness of the deposited film. This indicates that the column of MnGa grown atop a terrace of Mn_3N_2 is a relatively unperturbed crystallite with ordered layering and one crystallographic orientation.

Zheng *et al.* investigated the *out-of-plane* lattice parameter for $L1_0$-MnGa as a function of film thickness over 5–100 nm, with a corresponding variation of 3.32–3.71 Å in c[11]. This thickness trend is in good agreement with our *out-of-plane* spacing of 3.71 ± 0.01 Å.

Displayed in Fig. 6(a) is a large-scale STM image showing the surface morphology of the MnGa surface. Atomically smooth, flat terraces dominate the surface which is consistent with the layer-by-layer growth suggested by the streaky RHEED pattern during the growth, particularly during the final stages of growth. Hundreds of screw dislocations are evident in Fig. 6(a) manifested as small folds on the surface where several selected screw dislocations are indicated with a red-dashed circle in Fig. 6(a). A high-resolution image corresponding to a single screw dislocation is shown in the inset in Fig. 6(b).

Screw dislocations have been observed in other $L1_0$-ordered films. For the case of TiAl, Feng *et al.* and Jiao *et al.* showed that 1/2<110] screw dislocation was energetically most favorable, with screw dislocations able to cross slip into the (001) plane[40, 41]. However, unlike TiAl, the elastic constants of MnGa crystals are unknown which leaves dislocations in $L1_0$-MnGa based only on the empirical evidence, as we are unable to comment on the energetics of [001] screw dislocations. For consistency with other $L1_0$ dislocation analyses, the Burger's vector notation <hkl] means that permutations of h and k are allowed, but not l as indicated by the two different brackets[34].

The topographical AFM images shown in the work of Zheng et. al also revealed screw dislocations along [001], although they did not comment on these features in their report[11]. They observed a buckled surface with screw dislocations over a thickness range of 30–70 nm. At 100 nm thickness, their surface was no longer buckled and qualitatively agreed with our STM observations of surface morphology[11]. However, our surface exhibits smaller terrace widths, far more screw dislocations, and without the pile-up of 1/2<110] edge dislocations, which appear as steps of ∼4 nm height extending across the surface.

To understand the distribution of screw dislocations, as well as estimate the average distance between neighboring dislocations, a radial distribution plot (RDP) of screw dislocations is generated and shown in Fig. 6(c). To create the RDP we follow the method developed by J. C. Crocker *et al.* by counting the number of screw dislocations in an loop with thickness dR, at a distance R away from a reference screw dislocation[42]; we sum over X number of reference particles with an R_{max} = 100 nm and a dR = 10 nm.

The radial distribution plot of screw dislocations reveals a short range order with an average nearest neighbor distance of 15 nm. The short range order of screw dislocations extends to approximately 40 nm, but larger than this the random distribution of screws becomes equally likely. Error bars of the RDP are propagated from error in the loop area and error in the areal density of screw dislocations.

From the average separation between dislocations, an estimation of the total dislocation density (ρ) can be made via the formula:

$$\rho = \frac{2}{d^2}, \tag{2}$$

where d is the average distance between nearest dislocations and the factor of 2 comes from the relation of a surface dislocation density to a total bulk dislocation density[28]. As seen in Fig. 6(c) the RDP for screw dislocations has the first maximum at 15 nm which is used as an estimate for d which results in $\rho = 8.88 \pm 2.9(\text{x}10^{11})$ 1/cm^2 with an estimated 33% error in ρ.

The radial distribution of screw dislocations and together with Williamson-

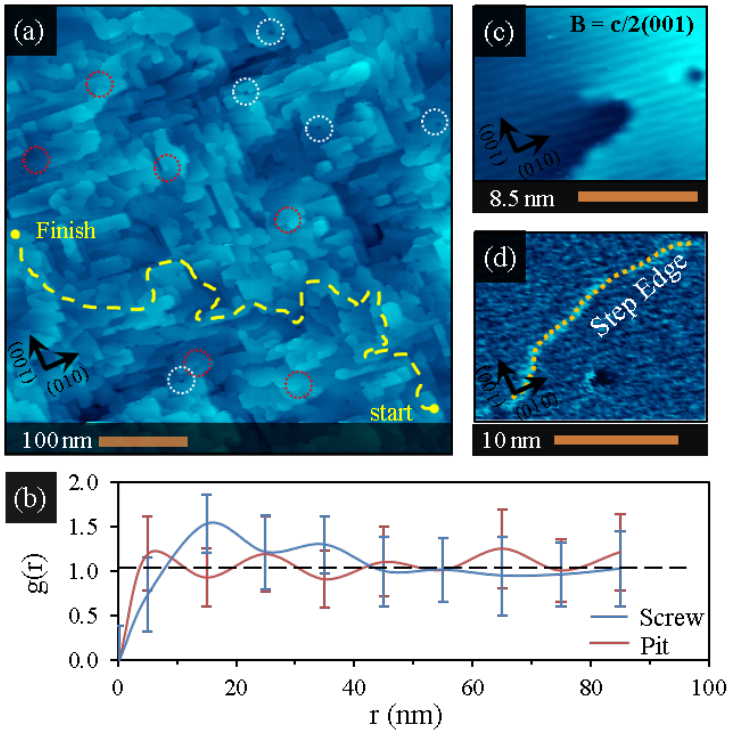

Figure 6: (a) Large scale STM imagine showing the morphology of the MnGa (001) surface. Hundreds of screw dislocations are visible as folds on the surface. Several example screw dislocations have been marked by by red dotted circles. Hundreds of small pits are also visible on the surface as black dots, which several examples are marked with white dotted circles. The yellow dashed line indicates a continuous path across the surface uninterrupted by an atomic step edge. (b) Radial distribution plots of screw dislocations and pits revealing short range order for the arrangement of screw dislocations and a random distribution of pits. (c) High resolution image of the effect of a screw dislocation with 1×2 row structure resolved. (d) Conductance map taken over a step edge showing no contrast change indicating compositional homogeneity across a monolayer-height step edge. Scanning parameters: (a,c) bias = -700 mV, setpoint = 1.0 nA (d) bias = -200 mV, setpoint = 1.0 nA

300 Hall analysis allow us to construct a model of the crystallite structure of the film, consisting of a collection of tall and thin (15 x 15 x 73 nm^3) crystallites with a 001 orientation. In conjunction, the RHEED, the Williamson-Hall, and RDP analyses verify the incorporation of dislocations to relax the misfit between

MnGa and Mn_3N_2. Although the dislocation density is high $\sim 10^{12}$ $1/cm^2$, so is the lattice misfit of 8 percent[39]. Furthermore, the results are consistent with the findings of Zheng *et al.* who found comparable FWHM values in XRD spectra of their MBE-grown MnGa films[11].

The MnGa(001) surface structures have been studied in detail experimentally and theoretically in our previous work[31, 33]. To recap the results of our previous studies as they are pertinent here, there are two lowest energy surface formations for the $L1_0$-MnGa (001) surface: an ideal 1×1 Ga termination and a Mn/Ga substitution in the 1×1 Ga termination forming a 1×2 row structure under very slightly Mn-rich conditions. Models of the two surface structures are shown in figure 7(a).

This alternating stacking of Mn and Ga layers creates a puzzle as one would expect an alternating composition across monolayer-height atomic steps and to observe terrace-specific surface structures and terrace-specific composition. However, we do not find evidence for this experimentally in the STM images. Theoretically, the Mn-terminations of the $L1_0$-MnGa (001) surface are highly unfavorable energetically compared to the Ga-terminations [31, 33]. The surface terminates in the lowest energy structure (Ga-terminations) via the screw dislocations. With such a high density of screw dislocations, it is possible for the surface to maintain the same Ga-termination while containing multiple single height atomic steps. It is even possible to traverse a 600 nm path across the surface [see Fig. 6(a)] without ever crossing a single step due to the high density of screw dislocations creating an Escher-type surface[43].

An STM conductance mapping is sensitive to the electronic density of states (DOS) which is dependent on the surface composition[18, 44]. Checking the DOS across a step edge can be an additional verification of any compositional variations. Conductance mapping is preformed utilizing a lockin amplifier technique[44]. We found no changes in the DOS for across the MnGa terrace steps, revealing no step-alternating compositional changes as shown in Fig.6(d).

Edge dislocations are visible in the STM images as kinks in the 1×2 surface structure as shown in Fig. 7(b). Shown in Fig. 7(a) is a derivative mode

STM image containing several edge dislocations. Edge dislocations similar to those observed in face-centered crystals are expected in $L1_0$-ordered materials which have a c:a ∼1:1 which is fairly close for the MnGa case (c:a = 0.93)[34, 45]. The energy of an edge dislocation is proportional to the square of the magnitude of the Burger's vector. With the a/2<110¿ being the shortest lattice translation vector, one expects $L1_0$-MnGa films to be populated with a/2<110] edge dislocations[34, 28]. Indeed, Zheng *et al.* observed via AFM a cross-hatch network in 100 nm thick $L1_0$-$Mn_{1.4}Ga$ films which they attributed to a pile-up of 1/2<110] edge dislocations.

We observe atomic-level edge dislocations of type 1/2<110] as an angled kink in the row structure extending across dozens of rows and even monoatomic step edges, as indicated by the arrows in Fig. 7(b). To create an atomic surface model of the 1/2<110] type dislocation, one has to keep in mind we are observing the effect of the edge dislocation perturbing the 1×2 Mn/Ga substituted surface structure. In part 1 of Fig. 7(c) an atomic model of a single row of Mn/Ga substitutions is displayed, where the Mn atoms are represented in red and Ga in blue. If the MnGa crystal is displaced by a a/2<110] edge dislocation through the row (as indicated by the dashed line) then the dislocated Mn atoms (orange colored) would occupy a non-equivalent position thus breaking symmetry of the 1×2 Mn/Ga substituted structure, as seen in part 2 of Fig. 7(c). As such, the position of the Mn substitution is located at the next-nearest equivalent position that would maintain the 1×2 surface structure. The incorporation into the next-nearest equivalent positions gives an additional shift in the position of the Mn-substituted atom, as seen part 3 of Fig. 7(c). Therefore, the kink in the row structure is the fingerprint of the 1/2<110] type edge dislocation. In Fig. 7(d) a derivative mode STM image is shown with our model of the 1×2 perturbed by a 1/2<110] edge dislocated surface overlayed along the rows containing a kink, giving good agreement with our experiment.

We determine that these kinks are due to bulk edge dislocations because the edge dislocation extends across a step edge as indicated in Fig. 7(b) by the white arrows. If these kinks were purely surface effects one would expect the

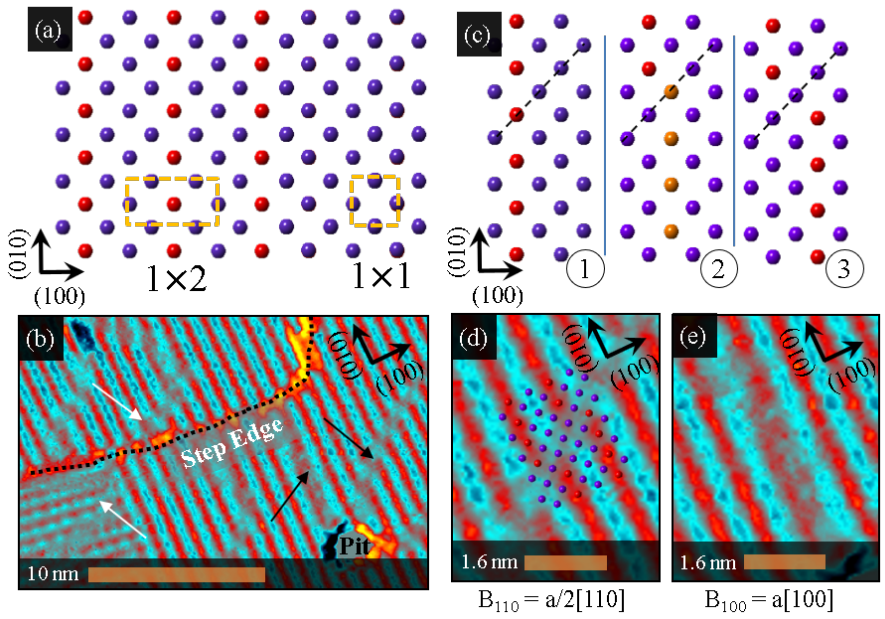

Figure 7: 1×2 and 1×1 surface models with STM image displayed in derivative mode showing an example of both 1/2<110] and <100] edge dislocations. (a) The models of 1×2 and 1×1 surface structures of the $L1_0$-MnGa(001). (b) Derivative mode STM image showing several edge dislocations. The white arrows mark a dislocation that goes across a step edge, while the black arrows indicate the two types of edge dislocations. Additionally, a ∼5 nm pit is visible in the bottom right corner. (c) 1×2 surface structure model of a 1/2<110] edge dislocation passing through a row. (d) A closeup of a kink in the row structure with the 1/2<110] dislocation model from part (c) overlaid on experimental data of the 1/2<110] edge dislocation. (e) A close up of a <100] edge dislocation showing a distortion in the row structure. bias = -700 mV, setpoint = 1.0 nA

kink to terminate an atomic step edge.

An edge dislocation in the <100] direction is observed as a distortion of the row structure along the length of the row, seen in Fig. 7(b). The <100] edge dislocation is observed much less frequently than the 1/2<110] dislocation; this is expected since the <100] dislocation has twice the energy of the lowest energy 1/2<110] edge dislocation.

In addition to edge and screw dislocations, the surface is densely packed

with small pits, where edge dislocations can be seen to terminate or connect as shown in Fig. 7(b). Zheng *et al.* found the formation of large pits (hundreds of nm in diameter) at a film thickness of ∼30 nm in $L1_0$-$Mn_{1.4}Ga$ films and also observed a competition between pit and dislocation formation as a function of thickness[11]. For our 73 ± 5 nm films ∼5 nm diameter pits were observed on the surface over a wide range. A large number of pits are observable as tiny black dots in the large-scale STM image, as seen in Fig. 6(a).

The pit diameter is significantly smaller than Zheng *et al.* reported for their films investigated via AFM. On the other hand, Zheng *et al.* observed that the pit formation diminished as the films thickened above 30nm and gave rise to an accumulation of edge dislocations in thick films of ∼100 nm[11]. Given that our films are 73 ± 5 nm in thickness, an intermediate combination of edge dislocations and pits would be expected[11].

To understand the ordering of the pit formation, an RDP of the pits is generated from the STM image shown in Fig. 6(a). From this RDP we determined that the pits develop across the surface of the sample randomly, as demonstrated by the essentially flat line with a value of 1 (to within error) across all measured distances. This indicates that there is no short or long range order, with a pit equally likely to be encountered anywhere on the surface, as seen Fig. 6(b).

3.3. Magnetism

A magnetic force microscopy (MFM) image showing the domain structure of the as-grown bilayer, is presented in Fig. 8(a), where the stripe-bubble pattern indicates an *out-of-plane* anisotropic behavior[46]. Observed in various $L1_0$-ordered magnetic films is a thickness dependence of the hysteresis shape. In Fig. 8(b) the *out-of-plane* hysteresis as measured by VSM has an interesting sheared and pinched shape which is known to occur for sufficiently thick $L1_0$ ferromagnetic films[47]. The sheared-pinched feature in the hysteresis is understood from micromagnetic theory to be related to the competing formation of bubble and stripe domains[47, 48, 49, 50]. Initially, when removing the saturating magnetic field, the creation of anti-parallel bubble domains is energetically

more favorable, until the bubble domains coalesce and form a network of stripes in the demagnetized state[47]. We observed a network of stripe domains, with some lingering bubble domains, as seen in Fig. 8(a) as anticipated from the work of Murayama[47].

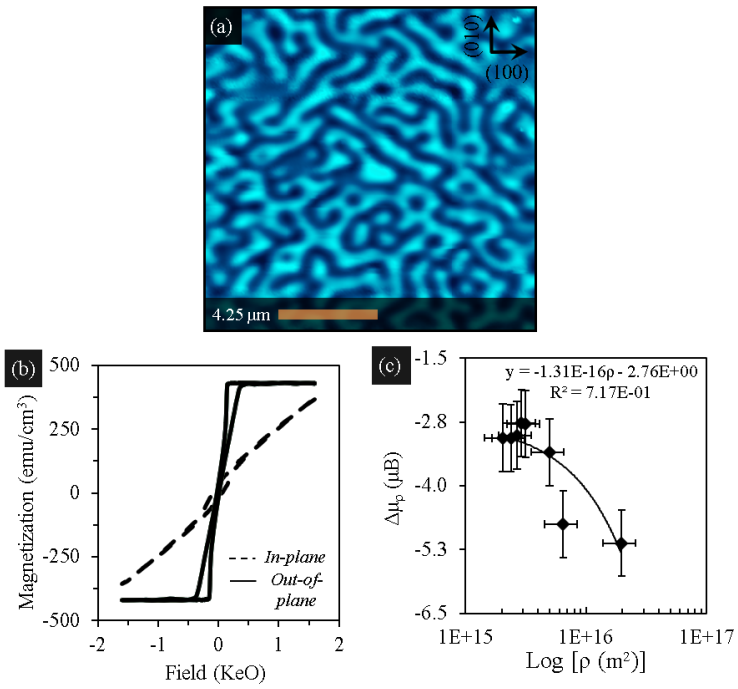

Figure 8: MFM image of the magnetic domain pattern and the results of the VSM measurements. (a) Stripe-bubble domain pattern indicative of an *out-of-plane* component of the magnetization. (b) *in-plane* and *out-of-plane* VSM loops of the bilayer showing a PMA nature of the material. (c) Empirical trend of the change in moment per unit cell versus log dislocation density determined from the data presented in the annealing study by Zheng *et al.*[11]

From the magnetic hysteresis loops (see Fig. 8(b)) the magnetic contributions per atom in a given unit cell is calculated by from the M_s and the unit cell volume ($V_{unitcell}$) via the relation:

$$\mu_{unitcell} = M_s \times V_{unitcell} \tag{3}$$

D. Kim *et al.* investigated the impact of uniform lattice strain on the mag-

netic moment per unit cell in the δ-Mn_x-Ga_{1-x} structures, resulting in a theoretical maximum of 9.88 μ_b per unit cell (or 2.47 μ_b per Mn atom) for the stoichiometric case[51]. Note D. Kim *et al.* used a conventional unit cell of the $L1_0$-MnGa (2 primitive stoichiometric unit cells stacked along the c-axis) for direct comparison to the off stoichiometric δ-Mn_x-Ga_{1-x} cases. They found that strains present in the lattice can lower the theoretical limit from 9.88 μ_b per conventional unit cell to 9.77 μ_b with reasonably linear trends of $\mu_{unitcell}$ versus strain[51].

Derived from the work of Kim *et al.* one arrives at a empirical equation:

$$\mu_{predicted} = \mu_{ideal} + \Delta\mu_{strain}, \tag{4}$$

where μ_{ideal} is the theoretical limit of the moment per unit cell set by the stoichiometry and $\Delta\mu_{strain} = \mu_{strain} - \mu_{ideal}$ with μ_{strain} being the theoretically calculated moment per unit cell under a given lattice distortion[51].

For the MnGa films investigated in this work, a $\mu_{unitcell}$ was determined to 5.53 ± 0.21 μ_b from our hysteresis measurements, substantially lower than the theoretical limit of 9.88 μ_b. Even when accounting for the lattice distortion a $\mu_{predicted} = 9.74$ μ_b is expected based on a linear extrapolation of measured moment versus lattice volume.

However, 5.53 μ_b is significantly lower than the strain-accounted case[51]. Zheng *et al.* investigated the effects of growth parameters (annealing temperature and thickness) on MBE grown $L1_0$-$Mn_{1.4}Ga$ films[11]. Using trends in the work of Zheng *et al.* for FWHM of XRD 002 peaks and M_s versus annealing temperature, we make a trend for $\Delta\mu_\rho$ versus ρ[11], where $\Delta\mu_\rho = \mu_\rho - \mu_{ideal}$ and μ_ρ is the moment per unit cell at a given ρ (where ρ is the film dislocation density). We determine this trend for $\Delta\mu_\rho$ versus ρ by processing the M_s and FWHM data as follows: first we calculate $\mu_{unitcell}$ from M_s via Eq. 3, giving us a plot of $\mu_{unitcell}$ versus annealing temperature. Then we use the Debye-Scherrer formula to estimate crystallite size from FWHM, and finally we convert crystallite size to ρ following Bindu *et al.* resulting in a ρ versus annealing temperature plot[38, 52]. Since both $\mu_{unitcell}$ and ρ are plotted versus same

annealing temperatures, we can finally plot $\mu_{unitcell}$ versus ρ. Finally, with μ_ρ versus ρ we take it one step further and plot $\Delta\mu_\rho$ versus ρ. The final plot is roughly a linear relation, see Fig. 8(c). This result leads one to an additional empirical term in Eq. 4 resulting in a final form:

$$\mu_{predicted} = \mu_{ideal} + \Delta\mu_{strain} + \Delta\mu_\rho. \tag{5}$$

We can then obtain $\Delta\mu_\rho$ from the straight line fit in Fig. 8(c) using the estimated ρ = 8.88 ± 2.9(x10^{15}) 1/m^2 for our film, which results in $\Delta\mu_\rho$ = -3.92 ± 0.55 μ_b. Combining this with the $\Delta\mu_{strain}$ = -0.15 ± 0.16 μ_b, is found to be $\mu_{predicted}$ = 5.82 ± 0.57 μ_b which is in very good agreement with the measure value of 5.93 ± 0.32 μ_b.

How the quality of the crystal can impact the magnetism of the film can be understood by realizing that the Mn magnetic moments in the $L1_0$ structure depends significantly on what atomic site the Mn occupies and by having the alternating layers of Mn and Ga. If a given sample does not have high-quality layering, but is still stoichiometric, the Mn atoms which adopted irregular $L1_0$ sites can couple antiferromagnetically, acquiring a ferrimagnetic behavior. We know from the XRD spectrum that we have reasonably high-quality layering but lack the 003 peak, indicating some layering mismatch. Our interface calculations directly show layering mismatch from vertical lattice misalignment between the Mn_3N_2(001) substrate and the MnGa.

Note that although the films in the work of Zheng *et al.* were not stoichiometric, we assumed that the change in moment versus ρ is sufficiently similar to our stoichiometric case. This assumption is motived by the work of Kim *et al.* who showed for the different concentrations of Mn in the δ-Mn_x-Ga_{1-x} structure that the change in moment versus strain was the same despite different compositions.

Additionally, the role of oxidation could potentially play a role in altering the magnetization. However, reports show that capped samples and uncapped samples are comparable, and even in the work of Mandru *et al.* uncapped ultra thin samples showed no evidence of oxygen degradation, having very large

moment per Mn atom of 4.84 ± 0.52 μ_b/Mn[4, 10].

Some MnGa films are known to exhibit perpendicular magnetic anistorpy (PMA)[4]. To quantify the PMA in our MnGa films, the uniaxial anisotropy constant K_u is determined from the area between the one set (e.g the right side) of the *out-of-plane* and *in-plane* hysteresis loops + the shape anistropy term via the approximate form[11]:

$$K_u = \frac{M_s H_{eff}}{2} + 2\pi {M_s}^2, \tag{6}$$

where H_{eff} can be estimated at the crossing point of the *out-of-plane* and *in-plane* loops[11]. In Fig. 8(b), the *out-of-plane* and *in-plane* VSM loops are plotted. The saturated magnetization M_s is determined from the *out-of-plane* loop and is measured from Fig. 8(b) to be 424 ± 1.0 emu/cc. H_{eff} is estimated to be 18721.0 ± 2.9 Oe. With the measured M_s and H_{eff}, K_u is calculated to be 5.10 ± 0.01 Merg/cc; this value is 1/3–1/4 smaller than other reports of $L1_0$-MnGa which is expected to be 15–20 Merg/cc for 73 nm thickness[11, 5]. For our 73 nm thickness and lower M_s value of K_u is is expected[11].

The angle of the easy axis (Θ) relative from the normal can be computed from the remnant magnetizations of the *out-of-plane* ($M_{r\perp}$) and *in-plane* ($M_{r\parallel}$) hysteresis loops via the formula:

$$\Theta = \arctan \frac{M_{r\parallel}}{M_{r\perp}}, \tag{7}$$

which results in $\Theta = 31.8 \pm 0.1°$. An *out-of-plane* easy axis is expected for MnGa thin films. The squareness and coercivity of the *out-of-plane* hysteresis loops depend on the thickness of the film[4, 47] The coercivity decreases dramatically as function of increasing thickness and the $M_{r\perp}$ no longer equals the M_s for films thicker than ∼60 nm, as also seen in our *out-of-plane* hysteresis in Fig. 8(b), thereby tilting the easy axis slightly *in-plane*.

Additionally, $\eta_\perp$-Mn_3N_2 is an antiferromagnet with a Neél point T_N = 624 °C while, $L1_0$-MnGa has a T_C = 354 °C, well below the Neél point creating the possibility of an unconventional EB system[16, 15, 17]. Strikingly and unexpectedly the *in-plane* loop is found to be shifted to left by 66 ± 21 Oe with a

coercivity of $H_c = 760 \pm 25$ Oe, as shown in Fig. 8(d). This is a strong indication of EB in the bilayer system. The ∼30% error of the EB field results from fitting straight lines to the low applied field regime of each branch of the hysteresis and using a linear regression to compute the y-intercepts, x-intercepts, and slopes with respective errors of each branch. Since the EB field is determined from a difference, i.e. the difference between the right and left coercivities, the relative error increases.

To compare to other EB systems, the energy shift ΔE created from the interface coupling is a way to compare different systems. This is given by the equation:

$$\Delta E = M_s t_{FM} H_e, \tag{8}$$

where M_s is defined as before, H_e is the shift of the hysteresis loop and t_{FM} is the thickness of FM layer. For our film, we calculate a $\Delta E = 0.2 \pm 0.1$ erg/cc, which when compared to other EB systems sits on the higher end of energy coupling[13], typical values are an order of magnitude lower.

This exciting finding opens new possibilities in these materials. Notably F. Jun-Ning et. al found unconventional EB using a non-stoichiometric MnGa and MnO in the nanoparticle state. Recently, other reports found EB with the θ phase of the Mn_xN_y system[19] which encouraged the exploration of $L1_0$-MnGa on Mn_3N_2 as a potential EB system[2]. Detailed explorations of the EB effects in this system are left to a future report as this work focused on the interfacing and the exchange coupling is only one aspect of the interfacing.

4. Conclusions

In conclusion, we revealed an epitaxial growth process resulting in tall columnar crystallites of $L1_0$-MnGa. Evidence of edge dislocations in the 1/2<110] and <100] directions and screw dislocations along the [001] was found in the STM images. The magnetic moment per unit cell ($\mu_{unitcell}$) was found to depend significantly on the dislocation density (ρ). We observed $\mu_{unitcell}$ lower by 3.92 $\pm$ 0.55 μ_b. This work uncovers some impacts that interfacing and disorder have

on the magnetic properties which in turn impacts the engineering of a film for spintronics or permanent magnetism.

Research supported by the United States Department of Energy, Oce of Basic Energy Sciences, Division of Materials Sciences and Engineering under Award # DE-FG02-06ER46317. Also, we acknowledge the use of WSxM software for image processing, and Fityk for curve fitting. We thank DGAPA-UNAM project IN100516 and CONACYT-Mexico Project 281052 for partial financial support. Calculations were performed in the DGCTIC-UNAM supercomputing center project LANCAD-UNAM-DGTIC-051. We thank the U.S. Department of Energy (DOE), Office of Science, Basic Energy Sciences, under Grant No. DE-SC0001304 for VSM measurements

References

[1] H. Meissner, K. Schubert, T. Anantharaman, The constitution and structure of manganese-gallium alloys, Proceedings Mathematical Sciences 61 (6) (1965) 340–367.

[2] F. Jun-Ning, L. Wei, G. Dian-Yu, M. Song, Y. Tao, Z. Xiao-Tian, D. Zhi-Ming, Z. Xin-Guo, Z. Zhi-Dong, Large coercivity and unconventional exchange coupling in manganese-oxide-coated manganesegallium nanoparticles, Chinese Physics B 23 (8) (2014) 087503.

[3] K. S. Stegen, Heavy rare earths, permanent magnets, and renewable energies: An imminent crisis, Energy Policy 79 (2015) 1–8.

[4] Z. Li-Jun, N. Shuai-Hua, Z. Jian-Hua, Recent progress in perpendicularly magnetized mn-based binary alloy films, Chinese Physics B 22 (11) (2013) 118505.

[5] L. Zhu, D. Pan, S. Nie, J. Lu, J. Zhao, Tailoring magnetism of multifunctional mn_xga films with giant perpendicular anisotropy, Applied Physics Letters 102 (13) (2013) 132403.

[6] A. A. El-Gendy, G. Hadjipanayis, Nanostructured $d0_{22}$-mn_3ga with high coercivity, Journal of Physics D: Applied Physics 48 (12) (2015) 125001.

[7] N. Al-Aqtash, R. Sabirianov, Strain control of magnetocrystalline anisotropy and energy product of mnga alloys, Journal of Magnetism and Magnetic Materials 391 (2015) 26–33.

[8] E. Lu, D. C. Ingram, A. R. Smith, J. Knepper, F. Yang, Reconstruction control of magnetic properties during epitaxial growth of ferromagnetic mn 3- δ ga on wurtzite gan (0001), Physical review letters 97 (14) (2006) 146101.

[9] W. Feng, D. Van Thiet, D. D. Dung, Y. Shin, S. Cho, Substrate-modified ferrimagnetism in mnga films, Journal of Applied Physics 108 (11) (2010) 113903.

[10] A.-O. Mandru, J. P. Corbett, J. M. Lucy, A. L. Richard, F. Yang, D. C. Ingram, A. R. Smith, Structure and magnetism in ga-rich mnga/gan thin films and unexpected giant perpendicular anisotropy in the ultra-thin film limit, Applied Surface Science 367 (2016) 312–319.

[11] Y. Zheng, G. Han, H. Lu, K. Teo, Annealing temperature and thickness dependence of magnetic properties in epitaxial l10-mn1. 4ga films, Journal of Applied Physics 115 (4) (2014) 043902.

[12] K. Wang, A. Chinchore, W. Lin, D. C. Ingram, A. R. Smith, A. J. Hauser, F. Yang, Epitaxial growth of ferromagnetic δ-phase manganese gallium on semiconducting scandium nitride (001), Journal of Crystal Growth 311 (8) (2009) 2265–2268.

[13] J. Nogués, I. K. Schuller, Exchange bias, Journal of Magnetism and Magnetic Materials 192 (2) (1999) 203–232.

[14] K. Sossmeier, L. G. Pereira, J. E. Schmidt, J. Geshev, Exchange bias in a ferromagnet/antiferromagnet system with tc tn, Journal of Applied Physics 109 (8) (2011) 083938.

[15] J. Cai, K. Liu, C. Chien, Exchange coupling in the paramagnetic state, Physical Review B 60 (1) (1999) 72.

[16] A. Berkowitz, G. Rodriguez, J. Hong, K. An, T. Hyeon, N. Agarwal, D. Smith, E. Fullerton, Antiferromagnetic mno nanoparticles with ferrimagnetic mn 3 o 4 shells: Doubly inverted core-shell system, Physical Review B 77 (2) (2008) 024403.

[17] P. Si, D. Li, J. Lee, C. Choi, Z. Zhang, D. Geng, E. Brück, Unconventional exchange bias in oxide-coated manganese nanoparticles, Applied Physics Letters 87 (13) (2005) 133122.

[18] K. Wang, A. R. Smith, Three-dimensional spin mapping of antiferromagnetic nanopyramids having spatially alternating surface anisotropy at room temperature, Nano letters 12 (11) (2012) 5443–5447.

[19] P. Zilske, D. Graulich, M. Dunz, M. Meinert, Giant perpendicular exchange bias with antiferromagnetic mnn, Applied Physics Letters 110 (19) (2017) 192402.

[20] M. Meinert, B. Büker, D. Graulich, M. Dunz, Large exchange bias in polycrystalline mnn/cofe bilayers at room temperature, Physical Review B 92 (14) (2015) 144408.

[21] J. Corbett, S. Pandya, A.-O. Mandru, J. Pak, M. Kordesch, A. Smith, Note: Advancement in tip etching for preparation of tunable size scanning tunneling microscopy tips, Review of Scientific Instruments 86 (2) (2015) 026104.

[22] H. Yang, H. Al-Brithen, E. Trifan, D. C. Ingram, A. R. Smith, Crystalline phase and orientation control of manganese nitride grown on mgo (001) by molecular beam epitaxy, Journal of applied physics 91 (3) (2002) 1053–1059.

[23] K. Alam, S. M. Disseler, W. D. Ratcliff, J. A. Borchers, R. Ponce-Pérez, G. H. Cocoletzi, N. Takeuchi, A. Foley, A. Richard, D. C. Ingram, et al.,

Structural and magnetic phase transitions in chromium nitride thin films grown by rf nitrogen plasma molecular beam epitaxy, Physical Review B 96 (10) (2017) 104433.

[24] P. Giannozzi, S. Baroni, N. Bonini, M. Calandra, R. Car, C. Cavazzoni, D. Ceresoli, G. L. Chiarotti, M. Cococcioni, I. Dabo, et al., Quantum espresso: a modular and open-source software project for quantum simulations of materials, Journal of physics: Condensed matter 21 (39) (2009) 395502.

[25] J. P. Perdew, K. Burke, M. Ernzerhof, Generalized gradient approximation made simple, Physical review letters 77 (18) (1996) 3865.

[26] D. Vanderbilt, Soft self-consistent pseudopotentials in a generalized eigenvalue formalism, Physical Review B 41 (11) (1990) 7892.

[27] H. J. Monkhorst, J. D. Pack, Special points for brillouin-zone integrations, Physical review B 13 (12) (1976) 5188.

[28] D. Hull, D. J. Bacon, Introduction to dislocations, Butterworth-Heinemann, 2001.

[29] C. R. Brundle, C. A. Evans, S. Wilson, Encyclopedia of materials characterization: surfaces, interfaces, thin films, Gulf Professional Publishing, 1992.

[30] J. Guerrero-Sánchez, A.-O. Mandru, K. Wang, N. Takeuchi, G. H. Cocoletzi, A. R. Smith, Structural, electronic and magnetic properties of mn 3 n 2 (001) surfaces, Applied Surface Science 355 (2015) 623–630.

[31] J. Guerrero-Snchez, N. Takeuchi, Formation of ferromagnetic/ferrimagnetic epitaxial interfaces: stability and magnetic properties, Under Review, Materials and Design.

[32] Y. Yamada-Takamura, Z. Wang, Y. Fujikawa, T. Sakurai, Q. Xue, J. Tolle, P.-L. Liu, A. Chizmeshya, J. Kouvetakis, I. Tsong, Surface and interface

studies of gan epitaxy on si (111) via zrb 2 buffer layers, Physical review letters 95 (26) (2005) 266105.

[33] J. Corbett, J. Guerrero-Sanchez, A. Richard, D. Ingram, N. Takeuchi, A. Smith, Surface structures of l10-mnga (001) by scanning tunneling microscopy and first-principles theory, Applied Surface Science 422 (2017) 985–989.

[34] F. Appel, J. D. H. Paul, M. Oehring, Gamma titanium aluminide alloys: science and technology, John Wiley & Sons, 2011.

[35] W. Pfeiler, Alloy physics: a comprehensive reference, John Wiley & Sons, 2008.

[36] A.-O. Mandru, J. Pak, A. R. Smith, J. Guerrero-Sanchez, N. Takeuchi, Interface formation for a ferromagnetic/antiferromagnetic bilayer system studied by scanning tunneling microscopy and first-principles theory, Physical Review B 91 (9) (2015) 094433.

[37] V. Mote, Y. Purushotham, B. Dole, Williamson-hall analysis in estimation of lattice strain in nanometer-sized zno particles, Journal of Theoretical and Applied Physics 6 (1) (2012) 6.

[38] S. G. Pandya, J. P. Corbett, M. Sundararajan, M. E. Kordesch, Stress and strain analysis for insb nanoparticles synthesized using inert gas condensation technique, Journal of Nanoscience and Nanotechnology 16 (9) (2016) 9838–9842.

[39] T. Metzger, R. Höpler, E. Born, O. Ambacher, M. Stutzmann, R. Stömmer, M. Schuster, H. Göbel, S. Christiansen, M. Albrecht, et al., Defect structure of epitaxial gan films determined by transmission electron microscopy and triple-axis x-ray diffractometry, Philosophical magazine A 77 (4) (1998) 1013–1025.

[40] Q. Feng, S. Whang, Deformation of ti–56 at.% al single crystals oriented for single slip by 1/2¡ 110] ordinary dislocations, Acta materialia 48 (17) (2000) 4307–4321.

[41] Z. Jiao, S. Whang, M. Yoo, Q. Feng, Stability of ordinary dislocations on cross-slip planes in γ-tial, Materials Science and Engineering: A 329 (2002) 171–176.

[42] J. C. Crocker, D. G. Grier, Methods of digital video microscopy for colloidal studies, Journal of colloid and interface science 179 (1) (1996) 298–310.

[43] http://www.mcescher.com/.

[44] A. R. Smith, Atomic-scale spin-polarized scanning tunneling microscopy and atomic force microscopy: A review, Journal of Scanning Probe Microscopy 1 (1) (2006) 3–20.

[45] A. A. Al Ghaferi, Deformation and dislocation tem image simulation in l 1 (0)-fepd (2006).

[46] A. Hubert, R. Schäfer, Magnetic domains: the analysis of magnetic microstructures, Springer Science & Business Media, 2008.

[47] Y. Murayama, Micromagnetics on stripe domain films. i. critical cases, Journal of the Physical Society of Japan 21 (11) (1966) 2253–2266.

[48] J.-U. Thiele, L. Folks, M. Toney, D. Weller, Perpendicular magnetic anisotropy and magnetic domain structure in sputtered epitaxial fept (001) l1 0 films, Journal of Applied Physics 84 (10) (1998) 5686–5692.

[49] M. Hehn, S. Padovani, K. Ounadjela, J. Bucher, Nanoscale magnetic domain structures in epitaxial cobalt films, Physical Review B 54 (5) (1996) 3428.

[50] V. Gehanno, Y. Samson, A. Marty, B. Gilles, A. Chamberod, Magnetic susceptibility and magnetic domain configuration as a function of the layer

thickness in epitaxial fepd (0 0 1) thin films ordered in the l1o structure, Journal of Magnetism and Magnetic Materials 172 (1-2) (1997) 26–40.

[51] D. Kim, J. Hong, L. Vitos, Epitaxial strain and composition-dependent magnetic properties of mn x ga 1- x alloys, Physical Review B 90 (14) (2014) 144413.

[52] P. Bindu, S. Thomas, Estimation of lattice strain in zno nanoparticles: X-ray peak profile analysis, Journal of Theoretical and Applied Physics 8 (4) (2014) 123–134.